Available online at www.sciencedirect.com
ScienceDirect
Comput. Methods Appl. Mech. Engrg. 283 (2015) 224–242
Computer methods in applied mechanics and engineering
www.elsevier.com/locate/cma

The use of discrete harmonics in direct multi-scale embedding of polycrystal plasticity

Nathan R. Barton[a,*], Joel V. Bernier[a], Ricardo A. Lebensohn[b], Donald E. Boyce[c]

[a] *Lawrence Livermore National Laboratory, Livermore, CA 94551, USA*
[b] *Los Alamos National Laboratory, Los Alamos, NM 87544, USA*
[c] *Sibley School of Mechanical and Aerospace Engineering, Cornell University, Ithaca, NY 14853, USA*

Received 7 April 2014; received in revised form 25 July 2014; accepted 14 September 2014

Abstract

We describe an approach for directly embedding polycrystal plasticity models in component scale calculations, with an emphasis on computational tractability. Previously, we have employed adaptive sampling to mitigate the computational cost of direct embedding, achieving two or more orders of magnitude in wall-clock speedup compared to more traditional approaches. However, in our previous work the crystal orientation distribution function (crystallographic texture) was not allowed to evolve significantly. Here we discuss an approach that allows for evolving texture by employing discrete harmonics, effectively decoupling considerations related to accuracy of integrals in the homogenization from those related to adequate representation of the evolving texture. We discuss the basic behaviors and convergence of the new polycrystal plasticity framework. Specific applications focus on the deformation of titanium, including the effects of twinning. Overall, the discrete harmonic based framework offers an attractive path forward for computationally efficient multi-scale embedding of polycrystal plasticity.

Keywords: Multi-scale; Polycrystal; Crystal plasticity; Constitutive models; Finite element method; Adaptive sampling

1. Introduction

There is longstanding interest in models that are able to capture anisotropic plastic flow, for example in simulations of metal forming [1–3]. Preferred crystallographic orientation in polycrystals is a principal source of anisotropy. This preferred orientation is sometimes referred to as crystallographic texture, and it is characterized by an orientation distribution function (ODF) [4]. The ODF is an important touchstone between experiment and simulation as it is easily measured by diffraction methods, with various methods appropriate to probing different sample volumes [5,6]. Models parameterized from a fixed crystallographic texture have been used to capture aspects of anisotropic flow, for example [2,7]. For scenarios involving tighter coupling with fine-scale state or for which precomputation is unattractive,

* Corresponding author. Tel.: +1 925 422 9426; fax: +1 925 423 3144.
E-mail address: barton22@llnl.gov (N.R. Barton).

http://dx.doi.org/10.1016/j.cma.2014.09.017
0045-7825/

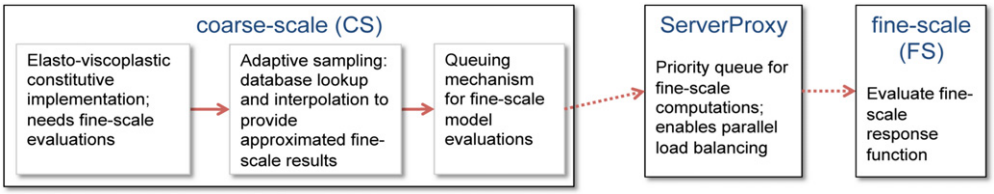

Fig. 1. Diagram outlining the call sequence by which the overall constitutive model obtains fine-scale model response information. Solid arrows indicate in-process function calls while dashed arrows indicate remote method invocation (RMI) [35]. In the case of the fine-scale (FS) evaluation itself, the remote method invocation is serviced using MPI-based parallel computing.

direct multi-scale embedding has been employed. However the computational cost of direct embedding of polycrystal plasticity is prohibitive, especially as one moves from relatively simple assumptions linking the deformation of the grains in the aggregate to models with higher fidelity and correspondingly higher computational expense [8–13].

To mitigate the cost of direct embedding, researchers have developed multi-scale embedding methodologies that employ adaptive sampling [14–19]. These techniques have some commonalities with *in situ* adaptive tabulation and similar schemes developed for modeling chemical kinetics [20–22]. Previous versions of the embedded polycrystal plasticity with adaptive sampling did not include texture evolution [17,23]. The primary thrust in the present work is to allow for texture evolution, including the effects of both crystallographic slip and deformation twinning, in a tractable multi-scale approach. Evolution of the texture, especially for materials that exhibit mechanical twinning, can significantly affect the evolution of flow stress at moderate levels of plastic deformation. It is worth noting that models to directly capture twin domain formation typically require fine computational grids and significant computational expense [24]. While there is utility in studies focused on details of twin formation, the focus here is on capturing the gross effects of texture evolution and twin formation on flow stress evolution.

The complexities of modeling texture evolution are well known [5]. For example, both spectral methods [25–29] and finite element based methods [30–32] have been employed to evolve the ODF. In spectral methods, the ODF is typically expressed in a Fourier series using symmetrized generalized spherical harmonics. Finite element schemes are often used over the Rodrigues parameter space. When accounting for mechanical twinning, the partial differential equation for ODF evolution becomes non-local, and such effects have been treated previously [8,33].

Here we use discrete harmonics based on a finite element discretization of Rodrigues space. This allows for independent control of the accuracy of ODF evolution and the accuracy of integrals over the orientation space. And, as shown below, we can capture salient features of texture evolution with many fewer parameters than are needed to track the orientations in a discrete aggregate based representation of a polycrystal. Nevertheless, the dimensionality of the polycrystal (fine-scale) response space remains relatively large—roughly 60 for the embedding in finite element calculations shown below. The input space includes the current state of the material and driving conditions such as stress state and temperature. The fine-scale model provides plastic deformation response and updated material state under these conditions. While the input dimension of the response space may be large, the portion of the response space probed in a given calculation tends to fall on a low-dimensional manifold [21,23]. The points on this manifold are not known ahead of time, motivating the use of an *in situ* adaptive sampling method that computes responses as needed.

Software modularity and multiple-program multiple-data (MPMD) parallelism are facilitated by the babel and co-op tools [34,35]. See [36,37] for a general discussion of advantages of MPMD parallelism for load balancing. Fig. 1 contains a diagram of the call sequence by which the overall constitutive model obtains fine-scale model response information. After development of the use of discrete harmonics in Section 2, we describe the constitutive model in Section 3. The fine-scale evaluations referenced in Fig. 1 amount to an evaluation or approximation of Eq. (24) as described below. In Section 4 we touch again on the decomposition of the workload onto computational resources, but we refer the interested reader to [23] for more details related to the use of computational resources. As described below, most of the calls to the adaptive sampling module result in an approximation of the fine-scale response based on previous evaluation data and do not require a new fine-scale model evaluation.

To demonstrate the convergence and efficacy of the discrete harmonic based approach, we show applications to the deformation of hexagonal α titanium, including mechanical twinning. This application is motivated by previously published work on this material [38]. Both Taylor (upper bound) and the more sophisticated but computationally intensive viscoplastic self-consistent (VPSC) type linking assumptions are used in the example calculations.

2. The use of discrete harmonics for texture evolution

Aspects of the application of discrete harmonics to texture evolution are provided here, with further details available in a companion paper [39]. The companion paper focuses on the mathematical and computational basis for the approach, while here we focus on the implementation and applications. These applications include the use of multiple linking assumptions for the polycrystal plasticity model, and include results for a material that undergoes deformation twinning. Some of the methodology related to discrete harmonics is discussed here for completeness.

Significant effort has gone into development of methods for evolving the probability density function for lattice orientation using partial differential equations over the appropriate space [8,25,31–33,40–43]. As described in various other works (for example [30–32,44]) the use of finite elements over Rodrigues space has several attractive properties for working with ODFs. Treatment of crystal symmetries is straightforward, resulting in planar boundaries to the fundamental region. Symmetrically equivalent values on opposite faces can be handled by condensation of redundant nodal degrees of freedom. Here we combine attractive features of the finite element approach with attractive features of harmonic expansions. The finite element machinery is convenient for evaluating integrals and operators. The harmonic expansion can provide a compact representation of the texture and its evolution. By bringing the two together we are able to independently control the accuracy of the numerical integration and the representation of the texture.

The ODF, A, satisfies a conservation equation

$$\frac{\partial A}{\partial t} + \mathrm{div}(A\mathbf{v}) = \Theta \tag{1}$$

in which $\mathbf{v}$ is the reorientation velocity field over the space. The use of such conservation equations for the ODF has been developed in previous work, for example [30–33,45]. At each point in the orientation space, this velocity field is directly related to the spin of the crystal lattice orientation. For example, in Rodrigues parameter space the reorientation velocity field takes the form [46]

$$\mathbf{v} = \frac{1}{2}\left(\boldsymbol{\omega} + (\boldsymbol{\omega}\cdot\mathbf{r})\mathbf{r} + \boldsymbol{\omega}\times\mathbf{r}\right) \tag{2}$$

with $\mathbf{r}$ being the Rodrigues vector encoding the lattice orientation [47,48] and $\boldsymbol{\omega}$ being the axial vector of the spin of the crystal lattice. That is, $\boldsymbol{\omega}$ comes directly from the usual kinematic expressions arising in crystal plasticity. At each point in the orientation space the $\boldsymbol{\omega}$ depends in general on the current stress condition; the local orientation; and the overall state of the material including the ODF, grain shapes, hardness state variables, and any other state quantities factoring into the polycrystal linking assumption. This dependence is described more fully in Section 3.3.

On the right-hand side of Eq. (1), Θ is zero for plastic deformation purely by crystallographic restricted slip without twinning. Deformation twinning abruptly reorients a portion of the crystal lattice and therefore transfers ODF density across the orientation space in a non-local manner [8,33]. With twinning, the form of the right-hand side of Eq. (1) is (see Equation 30 of [33]):

$$\Theta(\mathbf{r}) = \sum_{i=1}^{n_\mathrm{t}} A(\mathbf{r}_i^\mathrm{t}) w_i(\mathbf{r}_i^\mathrm{t}) - \sum_{i=1}^{n_\mathrm{t}} A(\mathbf{r}) w_i(\mathbf{r}) \tag{3}$$

where $w_i(\mathbf{r})$ is the volume fraction rate of twinning for twin mode i at lattice orientation $\mathbf{r}$ and $\mathbf{r}_i^\mathrm{t}$ is the orientation that contributes to $\mathbf{r}$ through activity of twin mode i. The first sum contains the source terms for orientations being produced by twinning and the second term contains the corresponding sink terms for orientations being depleted by twinning.

The finite element scheme follows from the weak form. Using weighting function ϕ and noting that the orientation space does not have a boundary

$$\int_{\Omega_\mathrm{fr}} \left(\phi\frac{\partial A}{\partial t} + \phi\,\mathrm{div}(A\mathbf{v})\right)\mathrm{d}\Omega = \int_{\Omega_\mathrm{fr}} \left(\phi\frac{\partial A}{\partial t} - A\mathbf{v}\cdot\nabla\phi\right)\mathrm{d}\Omega \quad \forall\,\phi \tag{4}$$

with Ω_fr denoting the fundamental region of the orientation space. For the special case of $\Theta = 0$ discretization produces the matrix equation

$$\mathsf{A}^+ = \mathsf{A}^- + \mathsf{L}^{-1}\mathsf{G}(\mathsf{A}^-\mathsf{v}^-)\Delta t \tag{5}$$

Table 1
Degree and dimension of the harmonics for hexagonal symmetry out to $d_{\mathrm{pf}} = 9$ (the maximum employed here). Note that d_{d} is the dimension of the subspace for the degree in question only, not including the dimensions of the subspace for lower degree harmonics.

PF degree (d_{pf})	0	2	4	6	7	8	9
quaternion degree (d_{q})	0	4	8	12	14	16	18
dimension (d_{d})	1	5	9	26	15	34	19

for the updated ODF nodal values A^{+}. In this equation L is the L^2 inner product matrix and G integrates a shape function gradient against a vector field over the mesh. In Eq. (5) we have also discretized in time according to a forward-Euler scheme, replacing $\frac{\partial A}{\partial t}$ with $(A^{+} - A^{-})/\Delta t$. Given a reorientation velocity field, Eq. (5) may be used directly to evolve the nodal values of the ODF [30,39]. Throughout this paper, sans-serif fonts (as in Eq. (5)) indicate quantities that are discretized using finite elements over Rodrigues parameter space.

Discrete harmonics form an attractive basis for representing and evolving the ODF. These are the discrete approximations to the spherical harmonics, which are themselves eigenfunctions of the negative Laplacian on the n-sphere. As discussed in [39], the discrete harmonics h_i are the eigenvectors of the generalized eigenvalue problem

$$\mathsf{H}\mathsf{u} = \lambda \mathsf{L}\mathsf{u} \tag{6}$$

in which H is the H^1 semi-inner product matrix. The h_i are orthonormal with respect to L and satisfy

$$\int_{\Omega_{\mathrm{fr}}} \mathsf{h}_j \mathsf{h}_k \mathrm{d}\Omega = \mathsf{h}_j \cdot \mathsf{L}(\mathsf{h}_k) = \delta_{jk} \tag{7}$$

with the lowest harmonic h_0 being uniform in value over Ω_{fr}.

All demonstration results shown here are for α titanium with hexagonal crystal symmetry. Table 1 shows the pole figure degree (d_{pf}), quaternion degree (d_{q}), and the dimension of the subspace (d_{d}) out to $d_{\mathrm{pf}} = 9$ [39]. Pole figure degree d_{pf} refers to the degree of the spherical harmonics on the usual sphere, and the quaternion degree is simply $d_{\mathrm{q}} = 2d_{\mathrm{pf}}$. The dimension of the subspace d_{d} is the number of independent harmonics on the orientation space for a given degree — d_{d} is not associated with the dimension of the Rodrigues space. For the true harmonics, all eigenvalues are the same for a given degree. Fig. 2 shows the eigenvalues of Eq. (6) for a finite element mesh with 3080 independent nodal degrees of freedom over the hexagonal fundamental region. This is the finite element mesh that is used for all of the results shown below. Fig. 2 also has lines that indicate the eigenvalues for the true harmonics of the given degree. The clustering of the eigenvalues within a degree gives an indication of how well the finite element mesh is able to approximate the true harmonics of that degree. Harmonics of higher degree have more fluctuations and are harder to capture.

Using the discrete harmonics we write

$$\mathsf{A} = \sum_{i=0}^{n_{\mathrm{h}}} c_i \mathsf{h}_i. \tag{8}$$

While the fidelity of the approximation of the true harmonics depends on the mesh being used, the discrete harmonics are always orthonormal so that $c_i = \int_{\Omega_{\mathrm{fr}}} \mathsf{A}\mathsf{h}_i \mathrm{d}\Omega$. The uniform 0th harmonic is the only one that integrates to a non-zero value and

$$\int_{\Omega_{\mathrm{fr}}} \mathsf{h}_j \mathrm{d}\Omega = 0 \quad \forall\, j \neq 0 \tag{9}$$

$$\frac{1}{c_0} = \int_{\Omega_{\mathrm{fr}}} \mathsf{h}_0 \mathrm{d}\Omega \tag{10}$$

so that the condition $\int_{\Omega_{\mathrm{fr}}} \mathsf{A}\mathrm{d}\Omega = 1$ is satisfied by construction given the fixed value of c_0. Thus the degrees of freedom for evolving the ODF are the discrete harmonic coefficients up to the desired degree excluding c_0. Alternatively, one

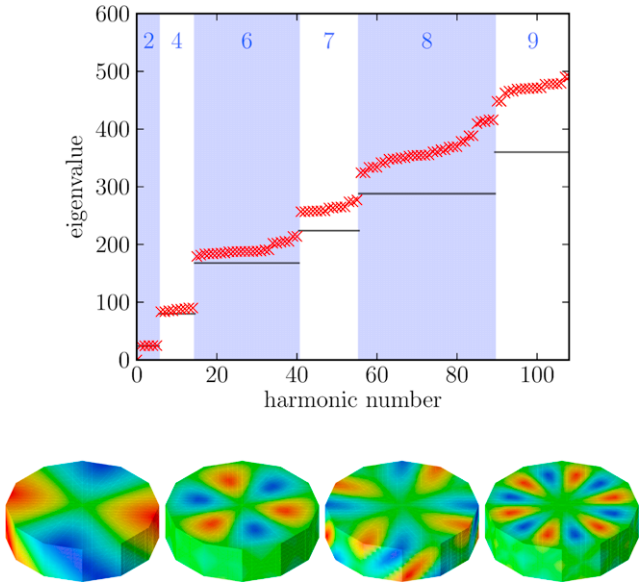

Fig. 2. Eigenvalues for the discrete harmonics up to $d_{\text{pf}} = 9$ for the mesh used for all results in this paper. The d_{pf} (pole figure degree) values are given across the top of the plot. Across the bottom, the figure also contains plots of some of the harmonic modes of various degree to illustrate the nature of the modes. These plots are over the hexagonal fundamental region of Rodrigues space.

could pick a general non-uniform function A that integrates to unity as the reference ODF, but then there could be variations that would not evolve because they are orthogonal to the basis being used.

The harmonic coefficients may be evolved directly. Given that the h_i are constant in time, the coefficients evolve according to:

$$\begin{aligned}\frac{\mathrm{d}c_i}{\mathrm{d}t} &= \int_{\Omega_{\text{fr}}} \frac{\partial A}{\partial t}\mathsf{h}_i \mathrm{d}\Omega \\ &= \int_{\Omega_{\text{fr}}} (\Theta - \operatorname{div}(A\mathbf{v}))\mathsf{h}_i \mathrm{d}\Omega \\ &= \int_{\Omega_{\text{fr}}} A\mathbf{v}\cdot\nabla\mathsf{h}_i \mathrm{d}\Omega + \int_{\Omega_{\text{fr}}} \Theta\mathsf{h}_i \mathrm{d}\Omega. \end{aligned} \tag{11}$$

As in Eq. (4), the application of integration by parts is for the special case of a space with no boundary. In the discrete form, the sum involving $\mathbf{r}_i^{\text{t}}$ (Eq. (3)) entails the computation of operators L_i^{t} such that

$$\int_{\Omega_{\text{fr}}} f(\mathbf{r})g(\mathbf{r}_i^{\text{t}})\mathrm{d}\Omega = \mathsf{f}\cdot(\mathsf{L}_i^{\text{t}}\mathsf{g}). \tag{12}$$

Note that the L_i^{t} depend on the finite element mesh employed and on the geometry of the twinning modes, but they do not depend on the degree of the discrete harmonic expansion. The discrete form of Eq. (11), with forward-Euler time discretization and including the effects of twinning, is then

$$c_i{}^{+} = c_i{}^{-} + \mathsf{h}_i \cdot \left[\mathsf{G}(\mathsf{A}^{-}\mathsf{v}^{-}) + \left(\sum_{j=1}^{n_{\text{t}}} \mathsf{L}_j^{\text{t}}(\mathsf{A}^{-}\mathsf{w}_j{}^{-}) - \sum_{j=1}^{n_{\text{t}}} \mathsf{L}(\mathsf{A}^{-}\mathsf{w}_j{}^{-})\right)\right]\Delta t. \tag{13}$$

Eq. (13) has clear similarities to Eq. (5) for the evolution over the nodal degrees of freedom in the finite element space. The terms involving w_j are simply the discrete form of Eq. (3). The $\mathsf{G}(\mathsf{A}^{-}\mathsf{v}^{-})$ term that is common to Eqs. (5) and (13) is the discrete form that arises from the divergence term in Eq. (1). The different evolution forms then involve different projections of this reorientation velocity field term. Like v, the fields of twin volume fraction rates w_j depend on the applied stress state and, in general, the current ODF and other state descriptors.

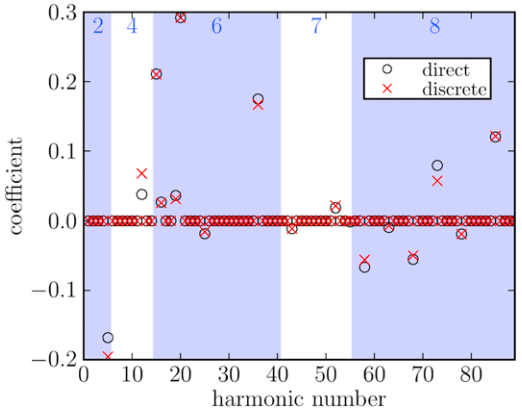

Fig. 3. Results for evolved harmonic coefficients using direct updating (Eq. (11)) versus projection from evolution of a set of discrete orientations. Both cases are based on a Taylor approach.

As a confirmation of the basic workings of the discrete harmonic based method, we compare results to a classical discrete aggregate type approach in Fig. 3. The reorientation velocity field over the hexagonal fundamental region is evaluated using a Taylor (upper bound) linking assumption [5]. Given the nature of the Taylor assumption, the velocity field for a given deformation mode is constant in time, which simplifies basic validation. To further simplify the validation, deformation is by restricted slip alone—twinning is not allowed. The specifics of the material model are largely irrelevant for this demonstration, as the Taylor linking assumption is used simply to generate a reorientation velocity field.

In the two simulations, the polycrystals begin with uniform ODFs and are strained in uniaxial tension to a true strain of 0.25. For the discrete aggregate calculation, an ODF is formed by centering Gaussian distributions around each of the discrete orientations and then projecting the result onto the harmonic coefficients. Given the smearing associated with the Gaussians and the differing approximations in the two methods, we do not expect to get precise agreement. The comparison in Fig. 3 and other such comparisons nevertheless serve to successfully validate the implementation. It is worth observing that only a small subset of the harmonic coefficients evolve to be non-zero. This is due to the high degree of symmetry in the both the deformation mode and the initial texture. One could reduce the size of the space for the texture by specializing the selection of harmonics to specific loading conditions, in rough analogy to a previously proposed approach [49]. But that is not done here as we seek a method that is applicable to more general loading scenarios in which the loading path is not known in detail ahead of time.

Texture evolution using the foregoing discrete harmonic based approach, especially under the rapid evolution driven by twinning, can drive the ODF negative over portions of the orientation space. We use finite elements with linear shape functions so that the extreme values of the ODF always occur at the nodes. Thus positivity can be checked by checking the nodal values of A. Positivity can then be enforced by truncating negative nodes to zero and rescaling the resulting A so that it once again integrates to unity. The truncated and rescaled ODF is used in the evolution equations and in the calculation of the weighting values for the integrals discussed below in Section 3.4. This straightforward procedure allows one to enforce positivity even for sharp initial textures or under strongly driven texture evolution. It is Eq. (13), with A appropriately truncated and rescaled as necessary, that we use for evolving the degrees of freedom in the applications shown in Section 4.

As a final note, from Eq. (13) we see that while the h_i are orthonormal the evolution of the c_i depends on the current ODF, reorientation velocity field, and twin fraction rates. Thus the c_i are coupled in their evolution and the evolved values of lower degree harmonics can change if the expansion is extended to include discrete harmonics of higher degree.

3. Constitutive model

The framework of the elasto-viscoplastic constitutive model is similar to that in [17] with extensions to allow for texture evolution and the use of more general theories for the fine-scale polycrystal plasticity model. Overall, the model shares many features with constitutive modeling frameworks described elsewhere [50–52]. The macroscale and thermo-elasticity aspects of the model are independent of the choice of Taylor [5] or VPSC [53] fine-scale models,

facilitated by a modular software implementation employing the babel [34] tool. Some salient features of the Taylor and VPSC linking assumptions are mentioned below in Section 3.4.

3.1. Kinematics

The kinematics for the constitutive model follow a standard multiplicative decomposition of the deformation gradient

$$\mathbf{F} = \mathbf{V} \cdot \mathbf{R} \cdot \mathbf{F}^{\mathrm{p}}, \tag{14}$$

in which $\mathbf{V}$ accounts for thermo-elastic stretch, $\mathbf{R}$ accounts for rotation of the material frame associated with the fine-scale material state, and $\mathbf{F}^{\mathrm{p}}$ accounts for plastic deformation. The velocity gradient $\mathbf{L} = \dot{\mathbf{F}} \cdot \mathbf{F}^{-1} = \mathbf{D} + \mathbf{W}$ is then

$$\mathbf{L} = \dot{\mathbf{V}} \cdot \mathbf{V}^{-1} + \mathbf{V} \cdot \hat{\mathbf{L}} \cdot \mathbf{V}^{-1} \tag{15}$$

$$\hat{\mathbf{L}} = \dot{\mathbf{R}} \cdot \mathbf{R}^{\mathrm{T}} + \mathbf{R} \cdot \bar{\mathbf{L}} \cdot \mathbf{R}^{\mathrm{T}}. \tag{16}$$

The fine-scale polycrystal model provides the plastic response in the form of the velocity gradient contribution $\bar{\mathbf{L}} = \dot{\mathbf{F}}^{\mathrm{p}} \cdot (\mathbf{F}^{\mathrm{p}})^{-1}$. For the plasticity models employed here, plasticity does not change the volume of the material so that $\mathrm{tr}(\bar{\mathbf{L}}) = 0$. The rest of the material model is handled at the coarse-scale. In the fine-scale model, plasticity is assumed to occur either by mechanical twinning or by restricted slip mechanisms on known crystallographic planes within the grains of the polycrystal.

As shown in [17], considerable simplification of the kinematics is possible based on assumptions about $\mathbf{V}$. Writing $\mathbf{V} \approx a(\mathbf{I} + \boldsymbol{\epsilon}^*)$ where $J = \det(\mathbf{V})$ and $a = J^{1/3}$ we assume that $\boldsymbol{\epsilon}^*$ is deviatoric and small. This results in:

$$\mathbf{R}^{\mathrm{T}} \cdot \mathbf{D}' \cdot \mathbf{R} = \frac{1}{a}\dot{\bar{\mathbf{V}}}' + \bar{\mathbf{D}}' \tag{17}$$

$$\frac{\mathrm{d}J}{\mathrm{d}t} = J\,\mathrm{tr}(\mathbf{D}) \tag{18}$$

$$\mathbf{R}^{\mathrm{T}} \cdot \mathbf{W} \cdot \mathbf{R} = \mathbf{R}^{\mathrm{T}} \cdot \mathbf{W}^{\mathrm{R}} \cdot \mathbf{R} + \bar{\mathbf{W}} + \frac{1}{a}\left[\bar{\mathbf{V}}' \cdot \left(\bar{\mathbf{D}}' + \frac{1}{2a}\dot{\bar{\mathbf{V}}}'\right) - \left(\bar{\mathbf{D}}' + \frac{1}{2a}\dot{\bar{\mathbf{V}}}'\right) \cdot \bar{\mathbf{V}}'\right] \tag{19}$$

where $\bar{\mathbf{V}} = \mathbf{R}^{\mathrm{T}} \cdot \mathbf{V} \cdot \mathbf{R}$, and $\mathbf{W}^{\mathrm{R}} = \dot{\mathbf{R}} \cdot \mathbf{R}^{\mathrm{T}}$. The kinematics retain desirable properties for large volume changes and for large rotations [17,52]. The appearance of the $\frac{1}{a}$ factor in Eq. (17) is directly related to the approximation $\mathbf{V}^{-1} \approx \frac{1}{a}(\mathbf{I} - \boldsymbol{\epsilon}^*)$ which is based on small $\boldsymbol{\epsilon}^*$. As detailed in [17], the time derivative of $\dot{\bar{\mathbf{V}}}'$ occurs before the bar operation so that extra time derivatives involving $\mathbf{R}$ do not appear.

We employ a logarithmic strain measure with a volumetric part that is exactly $\mathrm{tr}(\bar{\mathbf{E}}) = \ln(J)$. Consistent with the assumptions built into the kinematic approximations used in obtaining Eqs. (17) and (19), it is convenient to approximate the deviatoric part of the strain measure as $\bar{\mathbf{E}}' \approx \frac{1}{a}\bar{\mathbf{V}}'$. As with $\bar{\mathbf{V}}$, the bar in $\bar{\mathbf{E}}$ indicates rotation with $\mathbf{R}$, and use of the rotating frame simplifies the treatment of anisotropic elasticity.

The solution for Eq. (18) is, for constant $\mathbf{D}$ over a time step Δt,

$$J^{+} = \exp(\mathrm{tr}(\mathbf{D})\Delta t)\,J^{-}. \tag{20}$$

And with $\mathbf{W}^{\mathrm{R}}$ from Eq. (19) approximated as being constant over the time step we have

$$\mathbf{R}^{+} = \exp(\mathbf{W}^{\mathrm{R}}\Delta t)\mathbf{R}^{-}. \tag{21}$$

The evolution of $\mathbf{R}$ tracks the rotation of the frame associated with fine-scale material state, and thus captures rigid rotation of the texture.

With the decoupling of volumetric deformation into Eq. (20) and a forward-Euler approach to Eq. (21), we are left with the five dimensional non-linear system of equations in Eq. (17) to solve to complete the constitutive model update. Determining the partitioning of the deformation rate into rate of thermo-elastic stretch $\dot{\bar{\mathbf{V}}}'$ and plastic deformation rate $\bar{\mathbf{D}}$ requires information about the constitutive response of the material. As shown in Fig. 1 and discussed in Section 3.3, the fine-scale polycrystal plasticity model provides (by way of the adaptive sampling based interpolation) the values of $\bar{\mathbf{D}}$ and $\bar{\mathbf{W}}$ to help complete the constitutive description.

Due to the stiffness of the differential equation, we use a solution scheme that is fully implicit (backward-Euler) in $\bar{\mathbf{V}}$. A robust trust region subproblem based scheme [54] is used to solve the system of equations. With the exception of the derivatives of the response of the VPSC algorithm, all of the derivatives needed for the solution scheme are computed analytically. As in [17], full analytic derivatives are used throughout when employing a Taylor linking assumption.

3.2. Thermo-elasticity model

Thermo-elastic aspects of the model are not the emphasis here. It is worth noting that the anisotropic elastic moduli are evaluated from the initial ODF using an upper bound approximation. A straightforward modification of the scheme would allow for the elastic anisotropy to evolve as the texture evolves, but such effects are not the emphasis in Section 4 and for now we avoid the additional complexity.

With the Kirchhoff stress $\bar{\boldsymbol{\tau}} = J\bar{\boldsymbol{\sigma}}$ being work conjugate to the logarithmic strain to good approximation for small deviatoric strains [55,56] the elasticity model is phrased as

$$\bar{\boldsymbol{\tau}} = f_{\bar{\mathcal{K}}}(\bar{\mathbf{E}}, \theta, e) \tag{22}$$

with θ and e being the temperature and specific internal energy respectively. For applications in Section 4 temperature changes are small and temperature dependence of the elastic moduli may be neglected. The internal energy contributes to the stress through a Grüneisen parameter in the same way as discussed in [57]. This naturally gives rise to thermal expansion, and it is for this reason that we call $\mathbf{V}$ the thermo-elastic stretch.

3.3. Plasticity model, multi-scale embedding, and adaptive sampling

We now delve further into the details of the fine-scale response, how the response is computed, and how the response is manipulated through the call sequence outlined in Fig. 1. To complete the overall constitutive response, the fine-scale model provides information for $\bar{\mathbf{L}} = \bar{\mathbf{D}} + \bar{\mathbf{W}}$ and the evolution of the fine-scale state descriptors $\mathcal{H}$. Instead of providing $\bar{\mathbf{L}}$ directly, the fine-scale model provides parameters that can be used to compute $\bar{\mathbf{L}}$ through a non-linear function:

$$\bar{\mathbf{L}} = \bar{\mathbf{L}}_{\circ} \left| \frac{\|\bar{\boldsymbol{\tau}}'\|}{g} \right|^{1/m} \tag{23}$$

with the set of fine-scale response parameters determined from

$$\{\bar{\mathbf{L}}_{\circ}, g, m, \mathcal{H}^{+}\} = f_{\mathcal{Y}}(\bar{\boldsymbol{\tau}}', \mathcal{H}, p, \theta, \Delta t). \tag{24}$$

That is, the fine-scale model provides evaluations of $f_{\mathcal{Y}}$. The adaptive sampling method provides approximations of $f_{\mathcal{Y}}$ using interpolation schemes. In this functional form, $\bar{\mathbf{L}}_{\circ}$ provides directionality of $\bar{\mathbf{L}}$, g scales the material strength, and m approximates the material rate sensitivity. The behavior of these parameters is more amenable to interpolation by adaptive sampling than the highly non-linear behavior of $\bar{\mathbf{L}}$ itself. In contrast with the approach in [17], $f_{\mathcal{Y}}$ also provides the updated fine-scale state descriptors $\mathcal{H}^{+}$ over a time increment Δt for the given driving conditions. This choice is primarily motivated by a desire to isolate complexities in the update of $\mathcal{H}$ to the fine-scale model. However, like $\bar{\mathbf{L}}$, parts of $\mathcal{H}$ depend in a strongly non-linear manner on the inputs, especially $\bar{\boldsymbol{\tau}}'$. To improve performance of the sampling it may ultimately be desirable to update $\mathcal{H}$ using parameters from $f_{\mathcal{Y}}$ in nonlinear functions. It is not however clear that such an approach is tractable for general fine-scale models. For now we employ Eqs. (23) and (24) to demonstrate the approach with a comparatively simple formulation.

While the implicit solve of Eq. (17) requires only $\frac{\partial f_{\mathcal{Y}}}{\partial \bar{\boldsymbol{\tau}}'}$, the adaptive sampling modules require the derivatives of the full input–output relationship of $f_{\mathcal{Y}}$ in order to construct their interpolation functions [15,16]. As mentioned above, the derivatives in the Taylor case are done analytically, significantly mitigating the computational cost. But for VPSC finite differencing is used to perform parts of the derivative calculation for which analytic derivatives are not yet available. The wall-clock time for the finite-differencing is reduced using multiple-program multi-data (MPMD) parallelism to perform the finite differencing on remote processors in parallel (Fig. 1). For the results in Section 4 computing resources are used to reduce the wall-clock time of the fine-scale evaluation with derivative information to the equivalent of a single fine-scale evaluation.

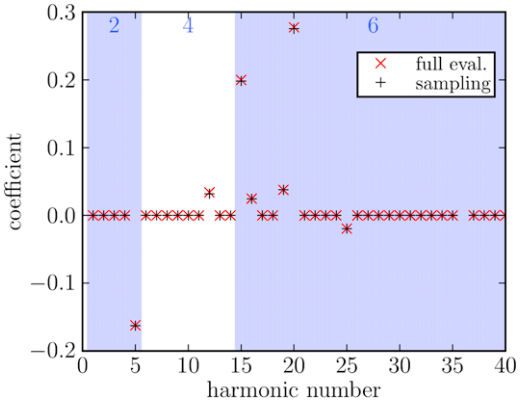

Fig. 4. Results for evolved harmonic coefficients using full fine-scale evaluations versus kriging based adaptive sampling. Both cases are based on a Taylor approach.

The modular implementation of the software facilitates switching among full fine-scale evaluations (no sampling), kriging based adaptive sampling [16], and an ellipsoid-of-accuracy based approach [15,21] that employs the same metric-tree database as in [16]. Fig. 4 compares the results of harmonic coefficients c_i evolved with a Taylor fine-scale model with either full evaluations or kriging based sampling. These types of comparisons between full evaluations and sampling were performed to verify accuracy of the sampling for a given set of numerical parameters in the sampling scheme. The sampling is generally found to control errors reliably in the approximation of $f_{\mathcal{Y}}$ and to produce acceptable wall-clock speedup in the calculations by virtue of the reduction in the number of fine-scale evaluations.

3.4. Fine-scale model

The queries to the fine-scale model are formulated completely from the arguments to $f_{\mathcal{Y}}$ in Eq. (24). The fine-scale servers depicted in Fig. 1 are launched and initialized with fixed data structures such as the G and the h_i at the beginning of the overall simulation, but the servers need not store any evolving fine-scale state information. Indeed, as the state is often updated by the adaptive sampling module without a call to a fine-scale server, and quadrature points at the coarse-scale are not associated with any particular fine-scale server, it does not make sense for the fine-scale servers to store evolving state information.

The modeling framework is exercised with both Taylor [5] and VPSC [53] style fine-scale polycrystal visco-plasticity formulations. In both cases, the formulations are simplified to have a single set of uniform hardness parameters for the entire polycrystal. As has been noted elsewhere[25,58,59], this type of approximation is sufficient to capture overall hardening effects especially in the absence of abrupt load path changes.

In the applications to titanium in Section 4 that make use of a VPSC linking assumption, there is a single scalar hardening parameter for each of the three deformation modes that are considered: prismatic slip $\{10\bar{1}0\}\langle\bar{1}2\bar{1}0\rangle$, pyramidal $\langle c+a\rangle$ slip $\{10\bar{1}1\}\langle\bar{1}\bar{1}23\rangle$, and tensile twinning $\{10\bar{1}2\}\langle\bar{1}011\rangle$. The $\mathcal{H}$ for the VPSC case is then composed of three hardnesses, a scalar accumulated shear value, six parameters that encode average grain shape, an accumulated twin fraction (for output purposes only), and the chosen number of discrete harmonic coefficients n_{h}. The framework could be extended to allow for distributions of the hardnesses over orientation space and each hardening parameter could then be represented by n_{h} additional coefficients. But for simplicity and to reduce the dimensionality of $\mathcal{H}$ such extensions are left for future work.

Given that each grain may deform differently under a VPSC scheme, VPSC models can be formulated to track distinct grain shape for each grain in a discrete aggregate. As part of the VPSC linking assumption, these grain shapes modulate the interactions of each grain with the rest of the polycrystal. Generally speaking, VPSC formulations can entail the tracking of significantly more history variables than a Taylor formulation. But here we focus on keeping the representation of the state compact, using for example an average grain shape instead of distinct shapes for various grains.

Under the VPSC scheme, the hardness state variables, grain shape, and ODF representation entering into $\mathcal{H}$ in Eq. (24) all influence the reorientation velocity field and the twin volume fraction rate fields. Through Eq. (13), these fields then determine the updated harmonic coefficients appearing as part of $\mathcal{H}^+$ in the output of Eq. (24). Thus for VPSC there is a fairly complete and complex coupling between the inputs and outputs to Eq. (24).

When using the Taylor linking assumption in Section 4 (and above in Section 2), we employ three types of slip systems: basal $\{0001\}\langle\bar{1}2\bar{1}0\rangle$, prismatic $\{10\bar{1}0\}\langle\bar{1}2\bar{1}0\rangle$, and pyramidal $\langle c+a\rangle$ slip $\{10\bar{1}1\}\langle\bar{1}\bar{1}23\rangle$. As indicated in Section 2, Taylor simulations are convenient for testing basic behaviors of the method, and they are conducted without twinning. As a further simplification in the Taylor case, a single scalar hardness parameter is tracked for the entire polycrystal, with fixed ratios of strengths among the slip system types. Also, the Taylor model is insensitive to grain shape.

Updates of the discrete harmonics in $\mathcal{H}^+$ are outlined in Section 2 and the update of the other entries in $\mathcal{H}$ follows standard formulations [5,53]. The computation of other quantities used in evaluating $f_{\mathcal{Y}}$ amounts to evaluating integrals of the form

$$\hat{f} = \int_{\Omega_{\text{fr}}} f(\mathbf{r}; \bar{\boldsymbol{\tau}}', \mathcal{H}, p, \theta) A(\mathbf{r}) \mathrm{d}\Omega \tag{25}$$

for some general function f over the orientation space. Like the integrals in Section 2, these integrals are performed using the finite element discretization of the fundamental region of Rodrigues space. The function f is computed at the symmetry-reduced nodal points on the mesh. The integral is then evaluated by a vector inner product involving the ODF values and weights that account for the mesh geometry and for the metric of the space. The weighting values are computed once and stored as they are fixed for a given mesh. Due to the coupling among crystal orientations in the response computed by VPSC, the f at each $\mathbf{r}$ depends on the full distribution of the current ODF which is provided to VPSC through the weighted ODF values at the nodal points (fixed orientations) over the mesh.

Results in Section 4 are generated using a finite element mesh with 3080 symmetry-reduced nodes, so that the fine-scale evaluations effectively make use of 3080 weighted discrete orientations. Alternatively, integrals could be computed by evaluating functions at the quadrature points. However with 18 432 elements in the mesh and 15 quadrature points in each element, that approach would result in significantly more computational work without a significant benefit in accuracy.

In Section 4 we see that one needs perhaps $n_{\text{h}} = 40$ to begin to capture reasonable texture evolution in hexagonal materials. While precomputation may be tractable for methods that do not evolve texture and are restricted to small-dimensional input spaces [7] or for Taylor type assumptions in which the response at each $\mathbf{r}$ decouples from the overall ODF [29], precomputation seems intractable in more general settings. For the case of VPSC, each evaluation requires roughly one processor-second. To cover a space with 60 input dimensions (for harmonics as well as $\bar{\boldsymbol{\tau}}'$, p, θ, and other $\mathcal{H}$ entries such as hardness variables) with eight points across each dimension one would require 10^{46} processor-years. Storage of the results spanning the full response space would also pose serious challenges. As stated in the introductory comments, such considerations drive the choice to employ adaptive sampling methodologies for concurrent multi-scale embedding.

Note that these comments about the motivation for adaptive sampling are made in the context of precomputation to span the full fine-scale response space. In contrast, VPSC type models are routinely used without adaptive sampling in simulations of the homogeneous deformation of a body, such as in idealizations of uniaxial tension and compression tests. For these types of calculations only a small number of VPSC evaluations is needed for each time step and the simplicity of direct embedding with full evaluations makes that approach attractive. Consideration of adaptive sampling is more relevant for macroscale calculations that probe a much wider portion of the fine-scale response space and require many fine-scale response evaluations each time step, such as in finite element simulations of forming operations [17].

As a final note about coupling to fine-scale models we recall from Section 2 that positivity of the ODF is enforced by truncating negative nodal values to zero and then rescaling. This procedure is performed before generating the weighting values at discrete orientations. As the weight values then depend on the rescaling factor, there are additional terms that appear in the chain rule expression for the derivatives of $f_{\mathcal{Y}}$ with respect to the harmonic coefficient entries in $\mathcal{H}$.

4. Results from application to titanium

To demonstrate the efficacy of the method, we apply it to deformation and texture evolution of hexagonal α titanium. The specific example calculations are motivated in part by the work described in [60,38], in which the starting material has been rolled and possesses a non-uniform initial ODF. As noted above, all ODF calculations make use of a finite element mesh with 3080 independent nodal degrees of freedom (3897 nodes total including redundant boundary nodes). Fig. 5 provides an example of the twinning inner product matrices L^{t}_j corresponding to the six distinct $\{10\bar{1}2\}\langle\bar{1}011\rangle$ tensile twin modes.

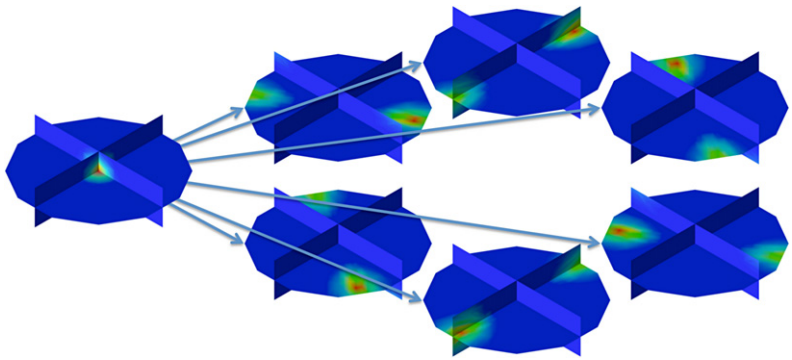

Fig. 5. Example of the action of the twinning operators for $\{10\bar{1}2\}\langle\bar{1}011\rangle$ tensile twinning in titanium. For a broad Gaussian distribution centered at the origin of the orientation space, the plots show the image of the Gaussian under operation of the six twinning modes. These results are depicted on slices through the hexagonal fundamental region of Rodrigues space.

Table 2
Convergence of evolved ODF versus degree d_{pf} for hexagonal symmetry using a Taylor linking assumption to effective plastic strain of 0.25 in uniaxial tension. See also Fig. 7.

PF degree	g error	ODF error
2	0.0110	0.468
4	0.00599	0.467
6	0.0125	0.234
7	0.0127	0.233
8	0.00237	0.160
9	0.000839	0.149

4.1. Convergence

Section 2 contains results for validating the discrete harmonic approach against results from a discrete aggregate based approach for a Taylor type linking assumption. Here we use a Taylor model to further explore convergence of results versus degree of the discrete harmonic expansion. And we also explore convergence for a VPSC type linking assumption in terms of predicted stress–strain results and pole figures. Given the focus in this section on convergence versus degree of the discrete harmonic expansion, simulations are conducted without adaptive sampling. That is, fine-scale calculations are done for every query of Eq. (24). Thus we avoid conflating accuracy concerns from the harmonic expansion versus the adaptive sampling. In this case without adaptive sampling, finite differencing of the VPSC fine-scale model evaluations is needed only to obtain the derivatives of the plastic deformation rate with respect to the deviatoric stress.

Basic convergence properties are first explored with a Taylor linking assumption without twinning. Results out to $d_{\text{pf}} = 9$ are shown in Table 2 and Fig. 7. These results are for a strain of 0.25 in uniaxial tension starting from a uniform ODF — for the same deformation condition as shown in Fig. 3. Results to a strain of 0.5 are similar in character but with more texture evolution so that one requires a higher degree in the expansion for the same level of accuracy in the flow stress response. Convergence is measured relative to evolution of the ODF using the full nodal degrees of freedom (Eq. (5)). Flow stress errors in Table 2 are normalized by the flow stress from the full nodal degree of freedom case, and ODF errors are computed using the L^2 inner product matrix. For comparison Fig. 7 shows the ODF evolved using the full nodal degrees of freedom, and the data for the full nodal evolution case are the same as in Fig. 3.

Over this range of the discrete harmonic expansion, flow stress response converges more quickly than sharp features of the evolved ODF. It is known that evolution of the ODF using a Taylor linking assumption rapidly produces sharp features in the texture [30], and it is expected that one requires expansion to a high degree to capture sharp features. It does however appear that flow stress behavior may be captured well without resolution of the sharpest features of the ODF. As noted in Section 2, expanding the basis to higher degree results in modifications to the lower degree discrete

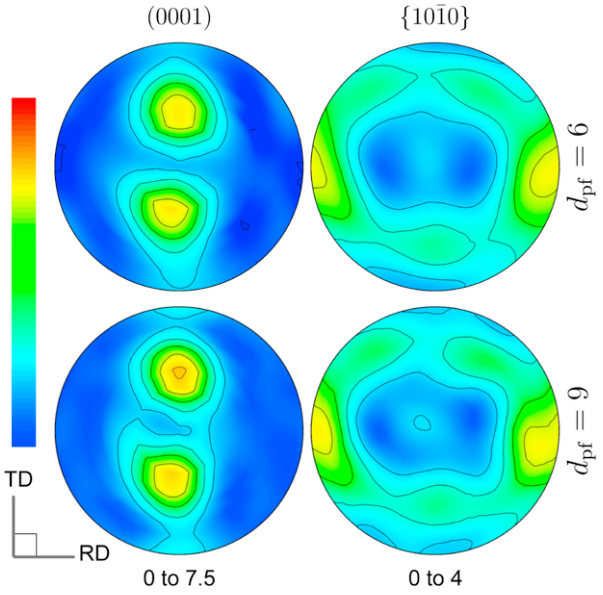

Fig. 6. Pole figures for the initial texture in the titanium as represented using harmonics to degree $d_{\mathrm{pf}} = 6$ and $d_{\mathrm{pf}} = 9$. Color scales are distinct for the (0001) and $\{10\bar{1}0\}$ pole figures.

harmonic coefficients — while the basis itself is orthonormal the evolution of the coefficients couples through the appearance of the current ODF in the evolution equations. This effect is seen in the convergence of the lower degree coefficients in Fig. 7.

Next, we explore convergence using a VPSC model for textured titanium with twinning. The parameters for the VPSC model are the same as those in [38]. The initial ODF is determined from pole figure values [38] and the ODF is projected onto the discrete harmonic modes to produce the initial c_i values for the fine-scale material state. Fig. 6 shows the reconstructed pole figures from ODFs with discrete harmonic expansions to degree $d_{\mathrm{pf}} = 6$ and $d_{\mathrm{pf}} = 9$. The pole figures are constructed using operators based on path integrals through the finite element discretization of Rodrigues space [44,43,61]. As seen in Fig. 6, expansion to degree $d_{\mathrm{pf}} = 6$ allows one to capture the major features of the ODF and the corresponding features in the pole figures.

Convergence behavior is examined in both tension and compression along the prior rolling direction (RD) in the material. Due to the starting texture of the material, tension versus compression along RD offers a strong contrast in the amount of twinning that is activated. Fig. 8 shows the stress–strain results and evolution of the twin volume fraction for the $d_{\mathrm{pf}} = 6$ case. For model validation, results are compared to predictions from a predominant twin reorientation (PTR) type of model that uses distinct hardness variables at each discrete crystal orientation. PTR is one of the twinning reorientation schemes proposed in [62] and consists in reorienting entire grains with high twinning activity into the orientation of their most active twin system, under the constraint that the total volume fraction of reoriented grains has to coincide with the actual twinned volume fraction calculated throughout the aggregate. In this way, the overall twinned volume fraction is accounted for, while the number of orientations remains constant. The PTR calculations also make use of a viscoplastic self-consistent linking assumption, but based on a discrete representation of the aggregate state and evolution. That is, based on a collection of grains with associated fixed volume fractions and evolving orientations.

The same model parameters are used in both the PTR simulations and the discrete harmonic VPSC based simulations. It would be possible to bring the models into closer agreement by adjusting parameters, but the comparison here highlights the mild differences due to differing treatments of the mechanics of twinning and hardening. The twinning mechanics in the discrete harmonic based scheme are more akin to a volume fraction transfer type scheme [8,33,62]. Comparison to the PTR scheme indicates that we capture the general features of deformation twinning while retaining attractive features for multi-scale embedding.

Figs. 9 and 10 show convergence of the stress–strain response and texture evolution with increasing degree of the discrete harmonics. In Fig. 9, the lower degree expansions are compared to the result for $d_{\mathrm{pf}} = 9$. Relative stress

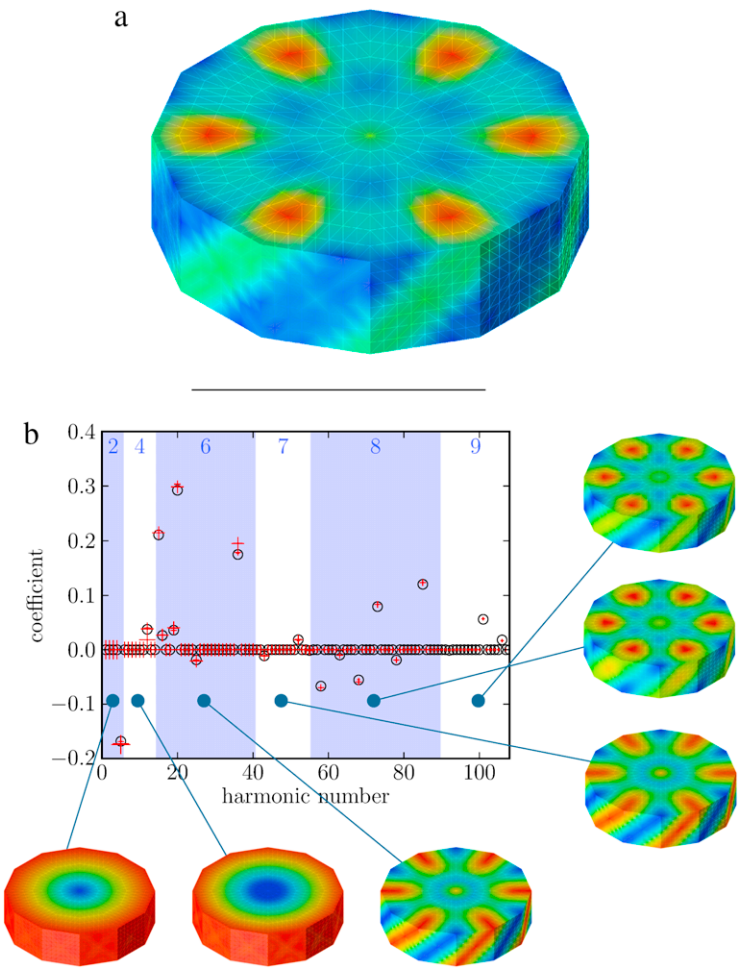

Fig. 7. Convergence of the evolved ODF versus degree d_{pf} for hexagonal symmetry using a Taylor linking assumption to effective plastic strain of 0.25 in uniaxial tension. See also Table 2. The ODF evolved with full nodal degrees of freedom is shown in (a) for comparison. In (b), the size of the + glyph for the harmonic coefficient is decreased as the degree of the discrete expansion is increased, and the coefficients projected from the full nodal evolution case are shown with open circles.

differences in Fig. 9 are normalized by the average flow stress in the $d_{\text{pf}} = 9$ simulation. In tension there is less twinning and the flow stress is well converged by $d_{\text{pf}} = 6$ out to a strain of 0.4. In compression the twinning drives more significant texture evolution. While $d_{\text{pf}} = 6$ appears to be sufficient out to strains of 0.2, higher degree may be required at larger strains depending on the desired level of convergence.

ODF convergence is assessed in Fig. 10 in terms of (0001) pole figures after strains of 0.2 and 0.4 in both tension and compression. Results are consistent with previous observations that flow stress response appears to converge more quickly than sharp features of the ODF. The differing amounts of twinning in tension versus compression clearly produce different textures as shown in the pole figures. The appearance of pole density near the prior RD direction under compression is directly related to the reorientation of the c axes of the crystals under deformation twinning.

4.2. Four point bend

To demonstrate the use of the discrete harmonic based approach in macroscale simulations, we conduct finite element simulations of four-point bend experiments discussed in [38,60]. Finite element simulations make use of the ALE3D code [63]. Note that the discretization of the physical space employs standard finite element machinery and we do not introduce any of the specifics here. The discretization discussed in the foregoing sections is strictly associated with the use of finite elements over Rodrigues space for the lattice orientations.

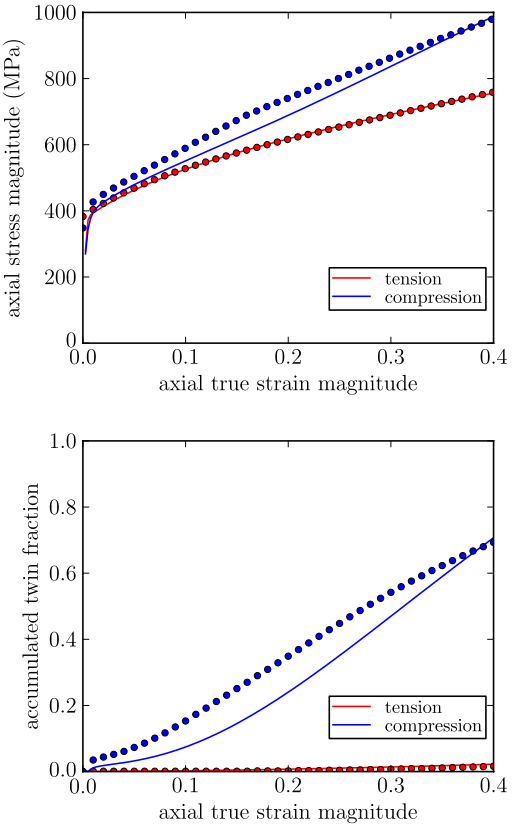

Fig. 8. Stress–strain results and evolution of the twin volume fraction for the $d_{\mathrm{pf}} = 6$ case (lines) for tension and compression along the prior rolling direction (RD), calculated with the VPSC approach. Results from the PTR scheme are shown (as points) for comparison.

Based on the results in Section 4.1 and the modest strains achieved in the bend simulations (less than 0.1), we use discrete harmonics up through $d_{\mathrm{pf}} = 6$ for which $n_{\mathrm{h}} = 5 + 9 + 26 = 40$ (see Table 1). Recall from Section 2 that the single harmonic coefficient h_0 for $d_{\mathrm{pf}} = 0$ is constant and does not contribute to n_{h}. These simulations are conducted using MPMD parallelism to decompose the workload, as in [18,23]. As noted in Section 3.3, this enables more rapid evaluation of $f_{\mathcal{Y}}$ (Eq. (24)) by finite differencing of the derivatives of the VPSC outputs that are not available analytically. Table 3 shows the allocation of computational resources among the executables, and the designations for the executables correspond to the components shown in Fig. 1. Note that the coarse-scale (CS) processes are 4× overloaded onto the compute cores. This is done to increase the number of concurrent fine-scale evaluation requests that can be generated and thus the overall throughput.

These calculations make use of the ellipsoid-of-accuracy based adaptive sampling approach [15]. We choose this method instead of the kriging based approach [16] because it is more conservative in its control of the interpolation error so that we can avoid numerical experiments to verify control of accuracy. The quasi-static four-point bend simulations involve the iterative solution of a non-linear global system of equations for the displacement field at each time step. The material stiffness matrix is algorithmically consistent, enabling quadratic convergence of the global system. As mentioned in [17], the sampling modules provide the necessary derivatives of the fine-scale response. And as noted in [13] the iterations for the global displacement field result in repeated fine-scale queries that are similar and this further improves the effectiveness of adaptive sampling module in reducing the fraction of expensive fine-scale computations performed.

Results of the bend simulations are shown in Figs. 11 and 12. These results correspond to cases 1 and 4 in [38]. In these two cases the samples are extracted from the rolled plate and bent in different directions, resulting in significant contrast in the mechanical response between the two cases. While the complete sample is shown in Fig. 11, only one quarter of the domain is simulated due to symmetries in the loading and, to good approximation, in the initial texture. Consistent with the initial texture, the deformation induced by the bending, and the unidirectional nature of twinning;

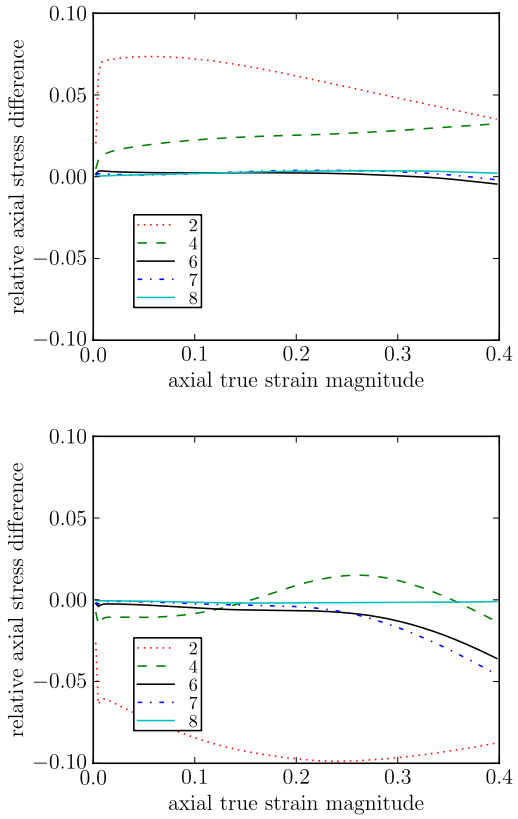

Fig. 9. Convergence of stress response versus degree d_{pf}, as compared to the $d_{\text{pf}} = 9$ case, for titanium using the VPSC linking assumption. Results are for uniaxial tension (above) and uniaxial compression (below).

Table 3
Executable instance and process allocation for the four-point bend simulations, on a machine with eight cores per node. The ServerProxy balances the $f_{\mathcal{Y}}$ evaluation workload among the fine-scale (FS) executables running VPSC. The adaptive sampling modules running as part of the coarse-scale (CS) processes produce a $f_{\mathcal{Y}}$ workload that is highly nonuniform across the parallel finite element domain decomposition and through simulation time [23]. See also Fig. 1 for a diagram outlining the call sequence interaction among components.

Component	Instances	Processes/instance	Total nodes
CS	1	64	2
ServerProxy	1	1	1
FS	10	48	60

for case 1 we see significant twinning only on the compressive side of the neutral axis. Note that the twin fraction plotted in Figs. 11 and 12 is evolved only as a convenience for tracking material response and does not feed back into the constitute evaluations. The twinning does however result in differences in the evolved texture, similar to differences shown in Section 4.1 for uniaxial tension versus compression. The shapes of the simulated final cross-sections shown in Fig. 12 are consistent with experimental observations for both case 1 and case 4. Capturing this type of anisotropic and directionally dependent material response is enabled by the crystal mechanics based plasticity model that includes a sound treatment of twinning. Differences in propensity to twin under the applied loading condition play a significant role in the different cross-sections shown in Fig. 12. As discussed in Section 4.1, the method is applicable out to much

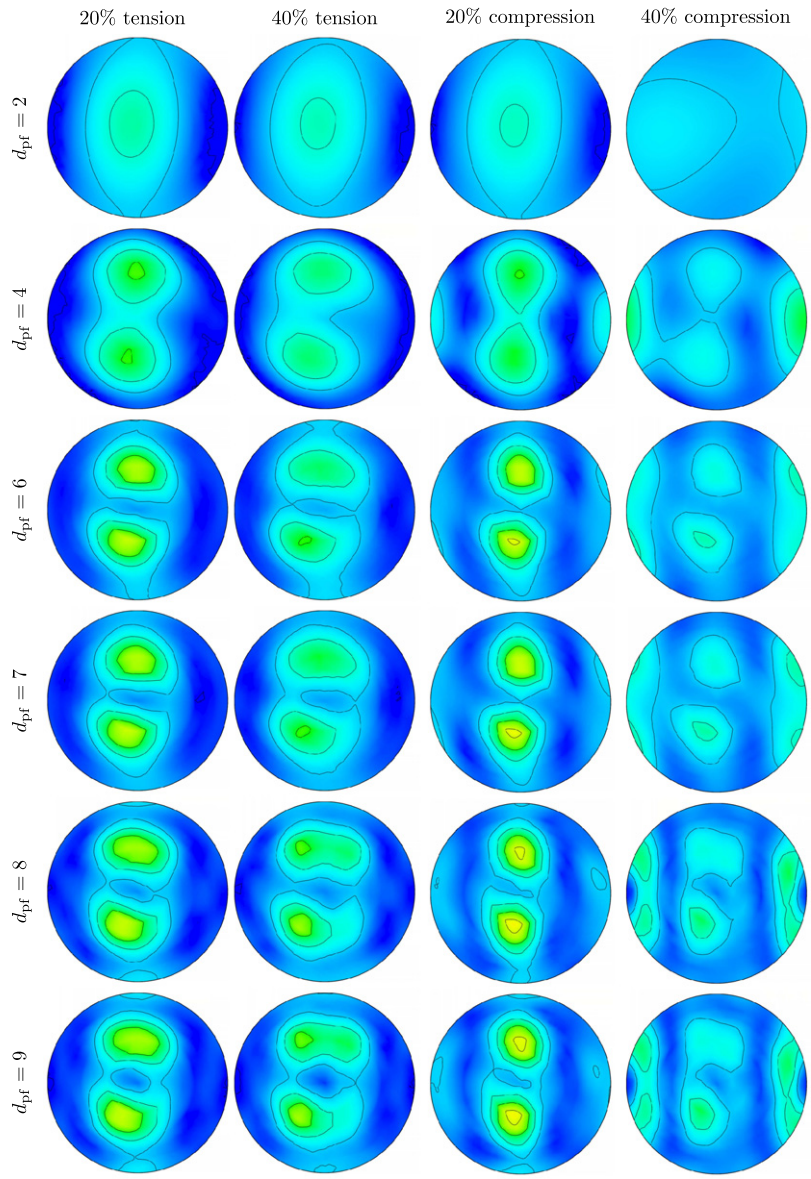

Fig. 10. Convergence of evolved ODF versus degree d_{pf}, as seen through (0001) pole figures, for titanium using the VPSC linking assumption.

larger strains, with the degree of the discrete harmonic expansion adjustable depending on the accuracy needed to capture texture evolution and its effects on material response for a given application.

The ratio of fine-scale evaluations ($f_{\mathcal{Y}}$) to fine-scale queries was about 0.1 in these four-point bend calculations. This is sufficient to provide significant wall-clock speedup, but is not nearly as low as has been reported in other applications of adaptive sampling [13,17,23]. However, the emphasis here is on demonstration of the discrete harmonic based approach and we therefore used a conservative sampling strategy.

5. Conclusions

A method for multi-scale embedding of polycrystal plasticity has been demonstrated, based on the use of discrete harmonics and finite elements over Rodrigues space. The method includes the effects of ODF evolution and convergence properties of the ODF evolution and flow stress response are attractive. Numerical performance is not an emphasis here, but the formulation allows for a compact representation of material state that is amenable to

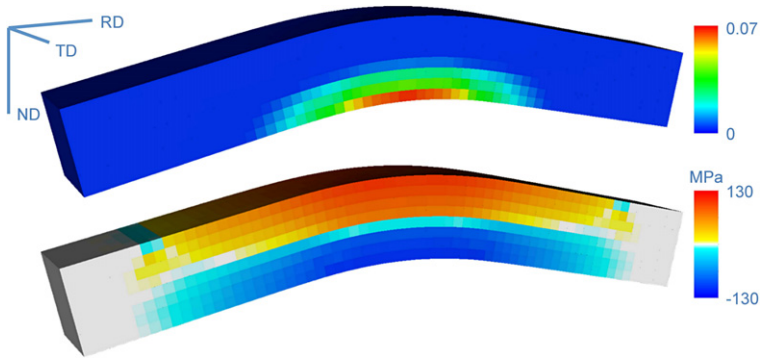

Fig. 11. Results from four-point bend simulation with VPSC: (top) twin fraction, (bottom) axial stress component. Sample orientation corresponds to case 1 in [38].

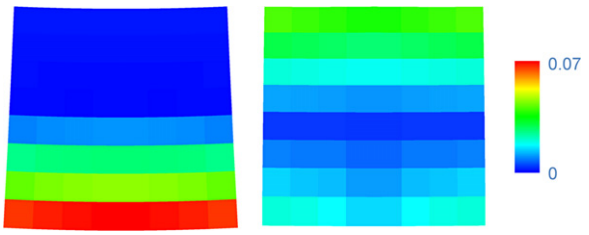

Fig. 12. Results from four-point bend simulations with VPSC: cross-sections at the mid-plane for sample orientations corresponding to (left) case 1 and (right) case 4 in [38], with plots showing simulated twin fraction over the cross-section.

use with adaptive sampling methodologies for more efficient multi-scale embedding. Focused work on numerical performance would be a useful avenue of further investigation. Computational cost aside, the memory footprint of the material state representation in the discrete harmonic based approach is small compared to that for a discrete aggregate representation of a polycrystal and this has advantages in some applications.

As expected, the response from the compact discrete harmonic representation of state differs somewhat from that predicted by a predominant twin reorientation model that tracks a much more extensive microstructural state. The current framework could be extended to include other fields, such as dislocation density or twin fractions, over the orientation space. However, results here indicate that the method as demonstrated captures the most significant effects of ODF evolution and its influence on flow stress response.

Acknowledgments

This work was performed under the auspices of the U.S. Department of Energy by Lawrence Livermore National Laboratory under Contract DE-AC52-07NA27344 (LLNL-JRNL-650713). Initial development of some of the capabilities used here was funded by the Laboratory Directed Research and Development Program at LLNL (04-ERD-102, 07-ERD-024). RAL and NRB further acknowledge support from the U.S. Department of Energy, Office of Science, Office of Advanced Scientific Computing Research, as part of the Exascale Co-Design Center for Materials in Extreme Environments.

References

[1] A.J. Beaudoin, P.R. Dawson, K.K. Mathur, U.F. Kocks, D.A. Korzekwa, Application of polycrystalline plasticity to sheet forming, Comput. Methods Appl. Mech. Engrg. 117 (1994) 49–70.
[2] P.J. Maudlin, S.K. Schiferl, Computational anisotropic plasticity for high-rate forming applications, Comput. Methods Appl. Mech. Engrg. 131 (1996) 1–30.
[3] P.R. Dawson, S.R. MacEwen, P.-D. Wu, Advances in sheet metal forming analyses: dealing with mechanical anisotropy from crystallographic texture, Int. Mater. Rev. 48 (2) (2003) 86–122.
[4] H.J. Bunge, Preferred orientation in deformed metals and rocks: an introduction to modern texture analysis, in: Representation of Preferred Orientations, Academic Press, Inc, 1985, (Chapter 4).

[5] U.F. Kocks, C.N. Tomé, H.-R. Wenk (Eds.), Texture and Anisotropy: preferred Orientations in Polycrystals and their effect on Materials Properties, Cambridge University Press, 1998.
[6] B. Adams, D. Field, A. Schwartz, M. Kumar (Eds.), Electron Backscatter Diffraction in Materials Science, second ed., Springer, 2009, ISBN 978-0387881355.
[7] Paul R. Dawson, Donald E. Boyce, Ryan Hale, John P. Durkot, An isoparametric piecewise representation of the anisotropic strength of polycrystalline solids, Int. J. Plast. 21 (2005) 251–283.
[8] R.A. Lebensohn, C.N. Tomé, A self-consistent viscoplastic model: prediction of rolling textures of anisotropic polycrystals, Mater. Sci. Eng. A175 (1994) 71–82.
[9] Gort.B. Sarma, Paul R. Dawson, Effects of interactions among crystals on the inhomogeneous deformations of polycrystals, Acta Mater. 44 (5) (1996) 1937–1953.
[10] R. Lebensohn, Modelling the role of local correlations in polycrystal plasticity using viscoplastic self-consistent schemes, Modelling Simul. Mater. Sci. Eng. 7 (1999) 739–746.
[11] Tong-Soek Han, Paul R. Dawson, A two-scale deformation model for polycrystalline solids using a strongly-coupled finite element methodology, Comput. Methods Appl. Mech. Engrg. 196 (2007) 2029–2043.
[12] R.A. Lebensohn, R. Brenner, O. Castelnau, A.D. Rollett, Orientation image-based micromechanical modelling of subgrain texture evolution in polycrystalline copper, Acta Mater. 56 (2008) 3912–3926.
[13] Nathan R. Barton, Joel V. Bernier, Ricardo A. Lebensohn, Anthony D. Rollett, Electron backscatter diffraction in materials science, in: Direct 3D Simulation of Plastic Flow from EBSD Data, second ed., Springer, 2009, ISBN 978-0387881355 (Chapter 11).
[14] S. Ashby, J. May, Petascale computing: Algorithms and applications, in: Multiphysics Simulations and Petascale Computing, Chapman & Hall/CRC Press, 2007.
[15] A. Arsenlis, N.R. Barton, R. Becker, R.E. Rudd, Generalized *in situ* adaptive tabulation for constitutive model evaluation in plasticity, Comput. Methods Appl. Mech. Engrg. 196 (2006) 1–13.
[16] J. Knap, N.R. Barton, R.D. Hornung, A. Arsenlis, R. Becker, D.R. Jefferson, Adaptive sampling in hierarchical simulation, Int. J. Numer. Methods Eng. 76 (4) (2008) 572–600.
[17] Nathan R. Barton, Jaroslaw Knap, Athanasios Arsenlis, Richard Becker, Richard D. Hornung, David R. Jefferson, Embedded polycrystal plasticity and adaptive sampling, Int. J. Plast. 24 (2) (2008) 242–266.
[18] Joel V. Bernier, Nathan R. Barton, Jaroslaw Knap, Polycrystal plasticity based predictions of strain localization in metal forming, J. Eng. Mater. Technol. 130 (2) (2008) 021020.
[19] L.Y. Lu, S.B. Pope, An improved algorithm for *in situ* adaptive tabulation, J. Comput. Phys. 228 (2) (2009) 361–386.
[20] S.B. Pope, Computationally efficient implementation of combustion chemistry using *in situ* adaptive tabulation, Combust. Theory Modelling 1 (1997) 41–63.
[21] M.A. Singer, S.B. Pope, Exploiting ISAT to solve the reaction–diffusion equation, Combust. Theory Modelling 8 (2) (2004) 361–383.
[22] L.E. Fried, The reactivity of energetic materials at extreme conditions, in: K.B. Lipkowitz, T.R. Cundari (Eds.), in: Reviews in Computational Chemistry, vol. 25, Wiley-VCH, 2007, pp. 159–184.
[23] Nathan R. Barton, Joel V. Bernier, Jaroslaw Knap, Anne J. Sunwoo, E. Cerreta, Todd J. Turner, A call to arms for task parallelism in multi-scale materials modeling, Int. J. Numer. Methods Eng. 86 (6) (2011) 744–764.
[24] N.R. Barton, J.V. Bernier, J.K. Edmiston, Bringing together computational and experimental capabilities at the crystal scale, in: AIP Conference Proceedings, in: Shock Compression of Condensed matter - 2009, vol. 1195, AIP, 2009, pp. 73–78.
[25] Mayeul Arminjon, Didier Imbault, An analytical micro-macro model for textured polycrystals at large plastic strains, Int. J. Plast. 10 (7) (1994) 825–847.
[26] S.R. Kalidindi, H.K. Duvvuru, Spectral methods for capturing crystallographic texture evolution during large plastic strains in metals, Acta Mater. 53 (2005) 3613–3623.
[27] Tony Fast, Marko Knezevic, Surya R. Kalidindi, Application of microstructure sensitive design to structural components produced from hexagonal polycrystalline metals, Comput. Mater. Sci. 43 (2) (2008) 374–383. ISSN 0927-0256.
[28] M. Knezevic, H.F. Al-Harbi, S.R. Kalidindi, Crystal plasticity simulations using discrete Fourier transforms, Acta Mater. 57 (2009) 1777–1784.
[29] Bogdan Mihaila, Marko Knezevic, Andres Cardenas, Three orders of magnitude improved efficiency with high-performance spectral crystal plasticity on gpu platforms, Int. J. Numer. Methods Eng. (2014) ISSN 1097-0207.
[30] Ashish Kumar, Paul R. Dawson, The simulation of texture evolution with finite elements over orientation space i. development, Comput. Methods Appl. Mech. Engrg. 130 (1996) 227–246.
[31] Ashish Kumar, Paul R. Dawson, Modeling crystallographic texture evolution with finite elements over neo-Eulerian orientation spaces, Comput. Methods Appl. Mech. Engrg. 153 (1998) 259–302.
[32] V. Sundararaghavan, N. Zabaras, Linear analysis of texture-property relationships using process-based representations of Rodrigues space, Acta Mater. 55 (2007) 1573–1587.
[33] Sergey Myagchilov, Paul R. Dawson, Evolution of texture in aggregates of crystals exhibiting both slip and twinning, Modelling Simul. Mater. Sci. Eng. 7 (1999) 975–1004.
[34] Thomas GW Epperly, Gary Kumfert, Tamara Dahlgren, Dietmar Ebner, Jim Leek, Adrian Prantl, Scott Kohn, High-performance language interoperability for scientific computing through Babel, Int. J. High Perform. Comput. Appl. 26 (3) (2012) 260–274.
[35] G. Kumfert, J. Leek, T. Epperly, Babel remote method invocation. In IEEE International Parallel and Distributed Processing Symposium, March 2007.
[36] David Jefferson, Brian Beckman, Fred Wieland, Leo Blume, Mike DiLoreto, Phil Hontalas, Pierre Laroche, Kathy Sturdevant, Jack Tupman, Van Warren, John Wedel, Herb Younger, Steve Bellenot, Distributed simulation and the time warp operating system. In 11th Symposium on Operating Systems Principles (SOSP), Austin, TX, 1987.

[37] Peter L. Reiher, David Jefferson, Dynamic load management in the time warp operating system, Transactions of the Society for Computer Simulation 7 (2) (1990) 91–120.
[38] Marko Knezevic, Ricardo A. Lebensohn, Oana Cazacu, Benoit Revil-Baudard, Gweénaëlle Proust, Sven C. Vogel, Michael E. Nixon, Modeling bending of α-titanium with embedded polycrystal plasticity in implicit finite elements, Materials Science and Engineering, A 564 (2013) 116–126.
[39] Donald E. Boyce, Joel V. Bernier, Nathan R. Barton, Discrete harmonics and their application to texture evolution, Journal of Applied Crystallography (2014) in preparation.
[40] K.-I. Kanatani, Distribution of directional data and fabric tensors, Internat. J. Engrg. Sci. 22 (2) (1984) 149–164.
[41] V.A. Lubarda, D. Krajcinovic, Damage tensors and the crack density distribution, Int. J. Solids Struct. 30 (20) (1993) 2859–2877.
[42] Vincent C. Prantil, James T. Jenkins, Paul R. Dawson, Modeling deformation induced textures in titanium using analytical solutions for constrained single crystal response, J. Mech. Phys. Solids 43 (8) (1995) 1283–1302.
[43] Joel V. Bernier, Matthew P. Miller, Donald E. Boyce, A novel optimization-based pole figure inversion method: comparison with WIMV and maximum entropy methods, J. Applied Crystallography 39 (5) (2006) 697–713.
[44] Nathan R. Barton, Donald E. Boyce, Paul R. Dawson, Pole figure inversion using finite elements over Rodrigues space, Textures Microstruct. 35 (2) (2002) 113–144.
[45] A. Clement, Prediction of deformation texture using a physical principle of conservatiol, Mater. Sci. Eng. 55 (2) (1982) 203–210.
[46] A. Kumar, P.R. Dawson, Computational modeling of F.C.C. deformation textures over Rodrigues' space, Acta Materialia 48 (2000) 2719–2736.
[47] F.C. Frank, Orientation mapping, in: J.S. Kallend, G. Gottstein (Eds.), Eighth International Conference on Texture of Materials (ICOTOM 8), Metallurgical Society, Santa Fe, NM, 1988.
[48] A. Morawiec, D.P. Field, Rodrigues parameterization for orientation and misorientation distributions, Phil. Mag. A 73 (4) (1996) 1113–1130.
[49] Shankar Ganapathysubramanian, Nicholas Zabaras, Design across length scales: a reduced-order model of polycrystal plasticity for the control of microstructure-sensitive material properties, Comput. Methods Appl. Mech. Engrg. 193 (45–47) (2004) 5017–5034.
[50] E.B. Marin, P.R. Dawson, On modelling the elasto-viscoplastic response of metals using polycrystal plasticity, Comput. Methods Appl. Mech. Engrg. 165 (1–4) (1998) 1–21.
[51] Nathan R. Barton, David J. Benson, Richard Becker, Crystal level simulations using eulerian finite element methods, AIP Conf. Proc. 712 (1) (2004) 1624–1629.
[52] Nathan R. Barton, Nicholas W. Winter, John E. Reaugh, Defect evolution and pore collapse in crystalline energetic materials, Modelling Simul. Mater. Sci. Eng. 17 (2009) 035003.
[53] R.A. Lebensohn, C.N. Tomé, A self-consistent anisotropic approach for the simulation of plastic deformation and texture development of polycrystals: application to zirconium alloys, Acta Metall. Mater. 41 (9) (1993) 2611–2624.
[54] J. Nocedal, S.J. Wright, Numerical Optimization, Springer, 2006.
[55] Morton E. Gurtin, Kathleen Spear, On the relationship between the logarithmic strain rate and the stretching tensor, Int. J. Solids Struct. 19 (5) (1983) 437–444.
[56] Anne Hoger, The stress conjugate to logarithmic strain, International J. Solids and Structures 23 (12) (1987) 1645–1656.
[57] R. Becker, Effects of crystal plasticity on materials loaded at high pressures and strain rates, Int. J. Plast. 20 (11) (2004) 1983–2006.
[58] D. Juul Jensen, N. Hansen, Flow stress anisotropy in aluminum, Acta Metall. Mater. 38 (8) (1990) 1369–1380.
[59] Matthew Miller, Paul Dawson, Influence of slip system hardening assumptions on modeling stress dependence of work hardening, J. Mech. Phys. Solids 45 (11/12) (1997) 1781–1804.
[60] Michael E. Nixon, Ricardo A. Lebensohn, Oana Cazacu, Cheng Liu, Experimental and finite-element analysis of the anisotropic response of high-purity -titanium in bending, Acta Mater. 58 (17) (2010) 5759–5767. ISSN 1359-6454.
[61] Nathan R. Barton, Joel V. Bernier, A method for intragranular orientation and lattice strain distribution determination, J. Appl. Crystallogr. 45 (2012) 1145–1155.
[62] C.N. Tomé, R.A. Lebensohn, U.F. Kocks, A model for texture development dominated by deformation twinning: application to zirconium alloys, Acta Metall. Mater. 39 (11) (1991) 2667–2680.
[63] A. Anderson, R. Cooper, R. Neely, A. Nichols, R. Sharp, B. Wallin, Users manual for ALE3D – an arbitrary Lagrange/Eulerian 3D code system. Technical Report UCRL-MA-152204, Lawrence Livermore National Laboratory, 2003.